ACS APPLIED MATERIALS & INTERFACES

RESEARCH ARTICLE

www.acsami.org

Three-Dimensional Photonic Crystal Fluorinated Tin Oxide (FTO) Electrodes: Synthesis and Optical and Electrical Properties

Zhenzhen Yang,[†,‡] Shanmin Gao,[†] Wei Li,[‡] Vitalii Vlasko-Vlasov,[‡] Ulrich Welp,[‡] Wai-Kwong Kwok,[‡] and Tao Xu*[,†,‡]

[†]Department of Chemistry and Biochemistry, Northern Illinois University, DeKalb, Illinois 60115, United States

[‡]Materials Science Division, Argonne National Laboratory, Argonne, Illinois 60439, United States

Supporting Information

ABSTRACT: Photovoltaic (PV) schemes often encounter a pair of fundamentally opposing requirements on the thickness of semiconductor layer: a thicker PV semiconductor layer provides enhanced optical density, but inevitably increases the charge transport path length. An effective approach to solve this dilemma is to enhance the interface area between the terminal electrode, i.e., transparent conducting oxide (TCO) and the semiconductor layer. As such, we report a facile, template-assisted, and solution chemistry-based synthesis of 3-dimensional inverse opal fluorinated tin oxide (IO-FTO) electrodes. Synergistically, the photonic crystal structure possessed in the IO-FTO exhibits strong light trapping capability. Furthermore, the electrical properties of the IO-FTO electrodes are studied by Hall effect and sheet resistance measurement. Using atomic layer deposition method, an ultrathin TiO_2 layer is coated on all surfaces of the IO-FTO electrodes. Cyclic voltammetry study indicates that the resulting TiO_2-coated IO-FTO shows excellent potentials as electrodes for electrolyte-based photoelectrochemical solar cells.

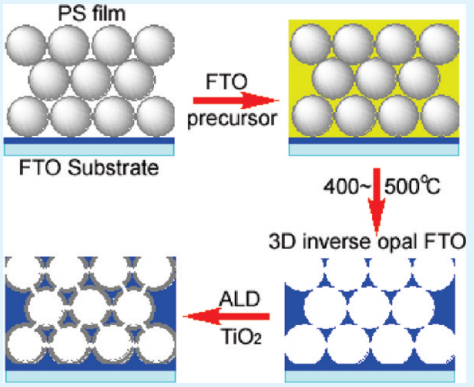

KEYWORDS: fluorinated tin oxide, electrode, inverse opal, photonic crystal, photoelectrochemical

INTRODUCTION

Transparent conducting oxides (TCO) are critical applied materials used in a wide range of optoelectronic devices,[1−8] such as solar cells[9] and thin film light emitting diodes, etc.[10] TCO such as indium tin oxide (ITO) and fluorinated tin oxide (FTO) are usually coated as planar two-dimensional (2D) transparent conductive films on flat transparent substrates to simultaneously allow both absorption/emission of light by the devices and the collection/injection of charges from/into the devices.[3] However, the conflicting requirements of the large optical thickness of the semiconductor layer and short transport distance for charges traversing the semiconductor layer consistently become the principle hurdle for the enhancement of the device efficiency.[11−14]

In particular, a thicker semiconductor layer is desired to carry more solar-absorbing p-n junctions or color centers for enhanced light harvesting. In a conventional PV configuration, the solar absorbing semiconductor layer is sandwiched between a flat 2D TCO thin film electrode and a counter electrode. This geometry leads to ineffective use of the vital TCO/semiconductor interface, where band bending occurs (region ∼50 nm thick). This band bending creates a built-in potential that provides a driving force to effectively separate electrons and holes.[15−18] Thus, efficient field-driven drift transport can occur at this TCO/semiconductor interface.[19] However, when a 2D TCO is used, the majority of charge transport pathways are far away from TCO/semiconductor interface, especially for a thick semiconductor layer, and diffusive transport dominates.[20−22] Charge separation and transport in the diffusion zone is very inefficient, because the random-walk electrons and holes suffer significantly from recombination because of the limited charge diffusivity and the long transport distance in thick semiconductor layers.[21−24] Moreover, defect sites in the semiconductor layer may also act as charge traps further slowing down the transport.[20−22,25] All these effects result in energy losses in photovoltaic devices, which reduce their performance in concert with the insufficient overlap between the absorption spectra of the PV semiconductors and the solar spectrum, and the rapid cooling of hot carriers, i.e., Shockley−Queisser Limit.[26,27]

Presently, a significant amount of effort in enhancing the charge transport efficiency is focused on improving of the semiconductor layer, by exploring new architectures with few crystal defects or new PV materials with the prospect of better charge diffusivity.[28−33] However, much less efforts have been devoted to the enhancement of the charge collection via innovations in the conventional 2D planar TCO-based electrodes.[34]

As a key component in many optoelectronic devices, TCO exhibits a much higher conductivity (>1 × 10^3 S/cm)[4,6,8] compared to traditional semiconductors used in the photoelectric

Received: December 16, 2010
Accepted: February 28, 2011
Published: March 11, 2011

structures, such as TiO_2 or ZnO (only a few S/cm even for single-crystal ZnO and anatase).[35−37] This is defined by the extremely high carrier concentration ($>1 \times 10^{20}/cm^3$)[4,8] and good carrier mobility in strongly doped TCO, which, due to its high density of states, is often treated as a metal.[24] In contrast, the carrier concentration in single crystals TiO_2 or ZnO is only $\sim 1 \times 10^{18}/cm^3$,[38] and the values are even lower in organic semiconductors.[22,39] Therefore, for the purpose of efficient charge transport, TCO would be a much more preferable material than most of solar absorbing semiconductors. Hence, it is a rational approach to place the TCO as close to the charge separation centers as possible to minimize the transport time in the poorly conductive (with respect to TCO) semiconductor layers.

To overcome this challenge, it is necessary to design a strategy to enlarge the TCO/semiconductor interface area so that a large portion of the semiconductor layer could be accommodated in the close proximity to TCO. In this way, the majority of charge transport pathways will be in the drift zone, in which transport is more efficient than in the diffusion zone. Geometrically, this can be realized by replacing the planar TCO electrode with a rough TCO film in a structure that will include a similar amount of semiconductor with a relatively thinner thickness.

In this work, we demonstrate a possibility to transform the conventional 2D TCO electrode into a 3D nanoarchitectured TCO with remarkably enhanced surface area. In addition, the transformation of the TCO film from the planar 2D to versatile 3D geometry enables us to intentionally incorporate special optical structures into the 3-D TCO film to synergistically enhance the light harvesting efficiency. For example, inverse opal, as a type of photonic crystals (PC), can enhance light harvesting due to the resonance of their structural and optical periodicity with the photon frequencies such that a longer matter−radiation interaction time can be achieved via multi-scattering in the PC.[40−42]

Below we report the synthesis and optical and electrical studies on nanoscale 3D inverse opal FTO (IO-FTO) electrode architectures with prospect of synergistic enhancement in both charge transport and light harvest, in contrast to their conflicting relation when a conventional 2-D TCO is used. Furthermore, the selection of FTO as a transparent electrode offers a better thermostability than ITO,[43,44] and reduces the material cost because of the higher natural abundance of fluorine compared to indium. These properties demonstrate the high potential of our structures for the scale-up fabrication and processes requiring the high-temperature treatment process. Moreover, for industrial applications, the simple solution chemistry synthesis of 3D FTO structures reported here avoids the use of toxic gaseous fluorine precursors.

EXPERIMENTAL SECTION

Materials. Monodispersed polystyrene nanospheres (PS, 2.50% solid latex, diameter 350 nm ±14 nm) were bought from Polysciences. $SnCl_4 \cdot 5H_2O$ (purity 99.99%), NH_4F (purity 99.99%), and ethanol (purity 99.5%) were purchased from Aldrich. All of these chemicals have been used without additional purification. The microscope glass slides (1 mm thick, Fisher Scientific) and FTO glass slides (2.2 mm thick, TEC 7 Pilkington) were used as substrates.

Fabrication of the PS Opal. The bare glass and FTO glass substrates used here were first sonicated in aqueous detergent (7X) solution for 15 min and rinsed with copious amount of pure water. The substrates were then soaked in 0.1 M HCl ethanol solution for 10 min under sonication to remove any metal contamination, and then rinsed again by pure water. The substrates were then dried in a stream of air, followed by O_2 plasma treatment for 10 min to remove any residual organic contaminants. The glass slides and the commercial FTO glass slides were placed on a leveled flat surface. Prior to use, the PS suspension were sonicated for 15 min to break down the aggregated particles. One-hundred microliters of PS suspension was dropped and spread uniformly on the substrates, which was left still for 10 min in air. After the solvent was evaporated, 3D-ordered PS latex film was formed on the glass slides. This process can be repeated to obtain thicker layers of PS opals.

Synthesis of 3D Inverse Opal FTO. In a typical preparation process of FTO precursory solution, 1.40 g of $SnCl_4 \cdot 5H_2O$ was dissolved in 20 mL of absolute ethanol. After 5 min of sonication, 0.24 g of saturated aqueous NH_4F (solubility is 45.3 g/100 mL at 20 °C) solution was added to the $SnCl_4$ in ethanol solution under vigorous stirring.[43,44] The resulting mixture was continuously sonicated for 20 min to obtain a clear solution. Subsequently, 60 μL of the FTO precursory solution was homogeneously spread on the as-prepared 3D PS template film. The solution penetrated the 3-D PS opal through the voids among the PS beads by capillary force. After drying at ambient temperature for 10 min, the film was further heated at 100 °C for another 10 min to remove any residual solvents. This process was repeated multiple times as needed to ensure the good filling of the voids by the FTO precursors.[47] With a heating rate of 1 °C/min, the resulting substrates were calcinated for 2 h under various temperatures in air for comparison.

Atomic Layer Deposition (ALD). ALD is the most suitable technique to produce high quality films with excellent reproducibility and superior conformal growth on various morphologies. The IO-FTO samples were coated with 10 nm TiO_2 by ALD (Sundew Technologies) at 180 °C by using $TiCl_4$ and H_2O as Ti precursor and oxidant, respectively. The pulse/dose/purge sequence for $TiCl_4$ is 20 ms/100 ms/1000 ms, and that for H_2O is 55 ms/200 ms/2000 ms. The growth rate was estimated to be approximately 3.3 Å/cycle.

Structural, Optical, and Electrical Characterization. SEM study was carried out on a field-emission scanning electron microscope (SEM, Hitachi-4700). X-ray diffraction (XRD) was performed on a Miniflex X-ray diffractometer. Optical transmission and reflection measurements were conducted on a UV−vis spectrometer (Ocean Optics Inc.).

The sheet resistance was measured by a four-probe method using a DC current source (Keithley 6221) and a nanovoltmeter (Keithley 196). In detail, four parallel thick indium strips (11 mm long and 1.2 mm wide) were pressed onto the surface of the IO-FTO film to make stable electrical contacts on the sample. A constant current of 100 mA was supplied between the two external current contacts placed 9 mm apart, and the voltage was measured between the two inner voltage contacts separated by a 3.5 mm gap.

Also, Hall Effect measurements were conducted to determine the carrier-type of the as-synthesized IO-FTO electrodes. Two parallel indium stripes on opposite sides of the sample were used as current electrodes and the Hall voltage was measured using two small contacts on the sides perpendicular to the current electrodes. The sample was placed on the flat surface of a permanent magnet yielding relatively homogeneous perpendicular field of 1.7 kOe over the sample area and the sign of the Hall voltage was measured with a current application of 100 mA. The polarity of the Hall voltage allowed us to determine whether the IO-FTO is n-type or p-type using a commercial n-type Si wafer as a reference.

The electrochemical cyclic voltammetry (CV) study was conducted in 0.1 M $LiClO_4$ and 1 mM ferrocene in acetonitrile[55] solution using a potentiostat (Gamry Reference 600). A platinum foil and an Ag/AgCl were used as the counter and reference electrodes, respectively, in all

Scheme 1. Growth Mechanism of Inverse Opal FTO and the Proposed Growth Mechanism of FTO Nanotubes[a]

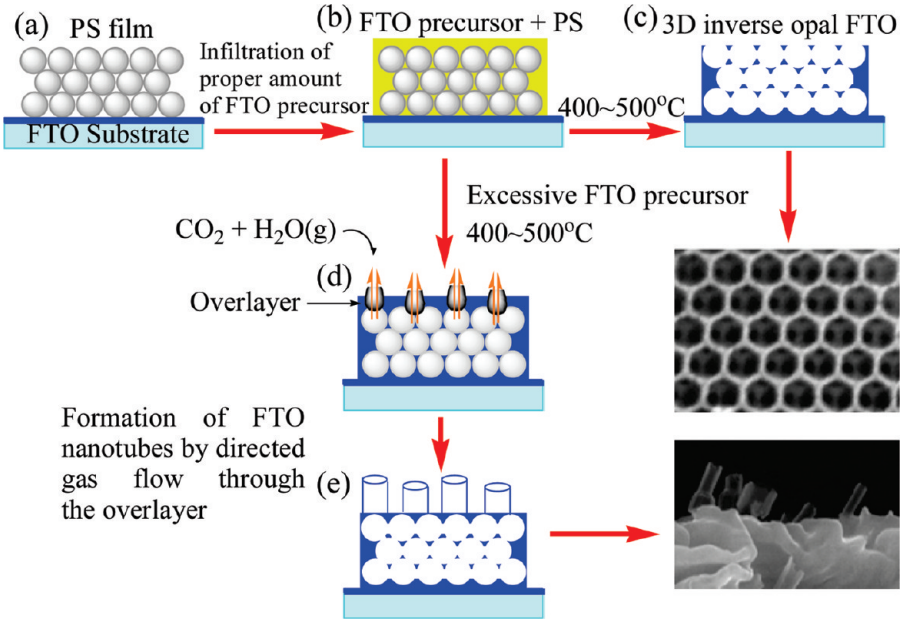

[a] (a) Self assembly of opal thin film composed of polystyrene (PS) microspheres on the FTO substrate. (b) FTO precursory material infiltration into the PS opal film to form composite structure. (c) Removal of PS template upon sintering at 400−500 °C. (d) The formation of overlayer on the very top of the film due to excessive addition of FTO precursor. (e) The formation of FTO nanotubes within one overlayer region that are directed along the gas, e. g., CO_2+H_2O flowing.

studies. Commercial Bare FTO glass (area = 1 cm^2), IO-FTO/FTO glass and TiO_2−IO-FTO/FTO glass were studied as the working electrode, individually.

RESULTS AND DISCUSSION

Synthesis and Structural Characterization of 3D IO-FTO Electrodes. Synthesis of the IO-FTO electrodes was conducted through a PS beads-templated method[41,45−47] as elucidated in Scheme 1. First, PS nanobeads are self-assembled into an opal thin film on a planar FTO glass substrate as shown in Scheme 1a. Figure 1a shows the scanning electron microscope (SEM) image of a multilayer PS spheres. The PS spheres are nearly monodispersed with a diameter of about 350 nm. Figure 1b shows the SEM cross sectional image of a 5-layer PS opal film. The PS microspheres have self-aggregated into a face-centered cubic (FCC) structure. This is because the stacking of hard spheres in a close-packed FCC arrangement is the densest and most stable configuration. Some dislocations were also observed on both the surface and the bulk of the PS film. The structural stability of the film was further enhanced via heat treatment at 60 °C, which promotes the attachment of neighboring spheres.[48] In an ideal FCC structure, the spheres occupy 74% volume, leaving 26% space for infiltration.[49]

To establish the desired IO-FTO structure, a precursory solution of FTO was then infiltrated into the voids of the PS opal matrix(Scheme 1b). To achieve a high filling rate of the precursors in the voids, we adopted the layer-by-layer precursor deposition method.[47] A proper amount of FTO ethanol precursory solution composed of $SnCl_4$ and NH_4F was cast into the voids of the PS opal matrix. Upon the evaporation of the ethanol at room temperature, the deposited $SnCl_4$ was further hydrolyzed to SnO_2 at 100 °C under a humid environment.[50] This process can be repeated multiple times to ensure that all the voids are filled, although no excessive materials form an overlayer. Figure 1c shows the SEM image of the resulting PS multilayer after infiltration and heat treatment of the precursory solution.

Finally, the 3D IO-FTO electrodes were obtained by temperature-programmed calcinations of the precursor-filled PS opal matrix. PS spheres start decomposing at 300 °C and further elevation of temperature leads to the complete removal of the PS spheres. The formation of FTO from its precursor requires higher temperature above 400 °C (Scheme 1c).

Figure 2a presents a large area SEM top view image of a typical 3D IO-FTO structure. It shows that our method can produce a large domain area (~5 μm × 5 μm) of the IO structure with only few defects. Figure 2b exhibits a top view SEM image at high magnification. The top surface is composed of a closely packed, hexagonally ordered microporous FTO. The diameter of the pores on this top layer is about 300 nm. Considering the initial 350 nm diameter of the PS spheres, we estimate the calcination-induced shrinkage of the structure (the micropore diameter compared to that of the original PS spheres) to be about 14%. Such shrinkage is likely due to the loss of liquid volume within the precusor. The well-defined 3D-ordered micropores in the top layer of the 3D IO-FTO film connect the corresponding nanopores (of an average size of ~70 nm) in the sublayer through the necks/joints. These nanopores in the sublayer originate from the contact area between the PS spheres, which cannot be filled with the precursory material. The wall thickness between each micropore on the top layer is about 40 nm. The surface roughness factor (SRF, i.e., the ratio of effective surface area of the IO-FTO to the projected substrate area) of the IO-FTO film can be calculated. For a FCC structure, the SRF of each layer is $2\pi/(3)^{1/2}$ (see the Supporting Information). For N layers of FCC spheres, the value is just multiplied by N. So, in principle, for example, a 5-μm-thick, 3-D IO-FTO film with voids of

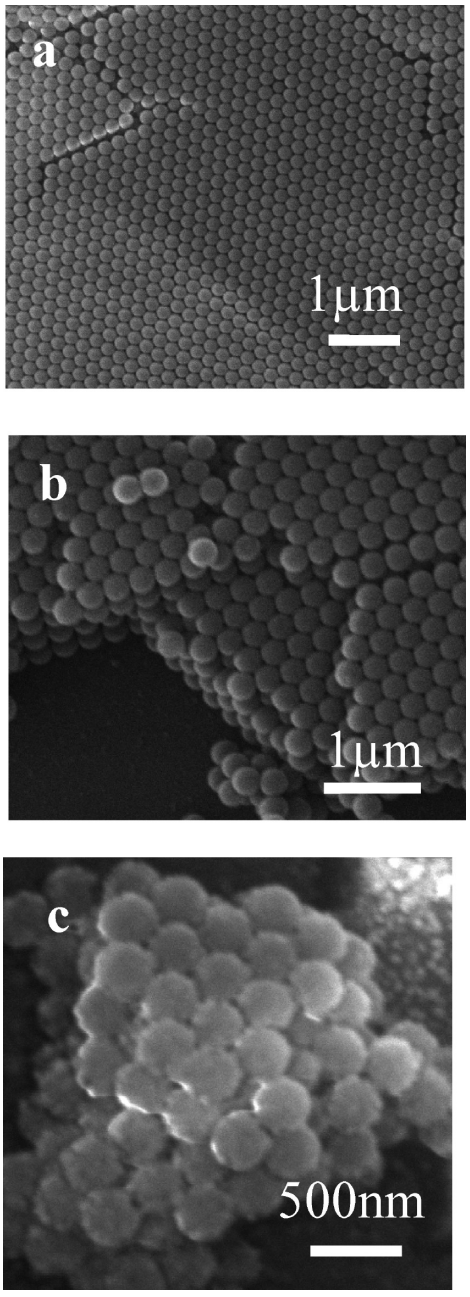

Figure 1. SEM images of template opal films. (a) PS template particle (350 nm) film(as prepared) on the substrate, showing dislocation on the surface; (b) the cross section of 5 layer-PS template on the substrate self-assembled as an FCC model; (c) PS/FTO precursor composite film on the substrate after complete infiltration, showing there is no overlayer coating.

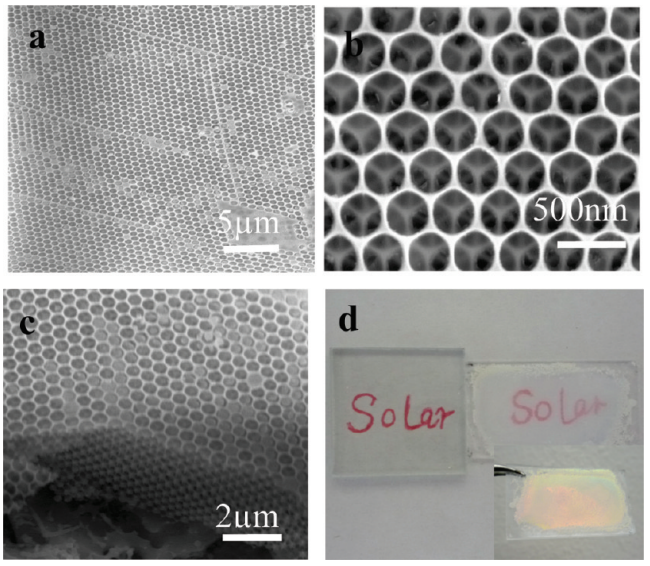

Figure 2. SEM images of as prepared inverse opal FTO under optimized condition. (a) A large topview image of a typical 3D IO-FTO structure. (b) A top-view SEM image at high magnification. The top surface is composed of a closely packed, hexagonally ordered microporous FTO. (c) Cross-section view of a fractured IO-FTO film on the FTO glass. (d) Digital images of a bare FTO glass and an IO-FTO film on glass with word "Solar" underneath each of the two substrates for comparison. The inset at right-lower corner captures the scattered light from the IO-FTO film at a tilted angle.

350 nm has about 17.5 layers. (see the Supporting Information). This is confirmed by the cross-section SEM image of a *ca.* 5 μm thick IO-FTO (Figure 2c). This yields a SRF of ~63.5 for such a 3-D IO-FTO film. This value of SRF is a significant enhancement in comparison to a planar FTO film, whose SRF is 1. The resulting FTO film is optically clear and macroscopically uniform as illustrated in Figure 2d (digital photos), where the word "Solar" written on the paper is clearly visible through a 5 μm thick IO-FTO film on a glass substrate. The inset photograph in Figure.2d shows the color of the scattered light[51] at a tilted angle, matching the stop-band of the prepared IO-FTO as discussed below.

Our experiments indicate that the relationship between the amount of precursory solution and the number of layers of the PS spheres exhibits a profound effect on the quality of the resulting IO-FTO film.[48] Typically, PS opals with fewer layers of spheres exhibit fewer cracks and dislocations. In addition, when the thickness of the PS opal template is fixed, the amount of the infiltrated precursory material will show two effects. If the precursory material is insufficient to fill all voids, the resulting IO-FTO film appears structurally imperfect (Figure 3a), and thin as shown in the cross-sectional SEM image (Figure 3b). However, when excessive amount of the precursory material is infiltrated, some patches of flakelike overlayers form on the top surface (Figure 3c). Further addition of precursors leads to an almost continuous and thicker film as shown in Figure 3d. By choosing proper infiltration of the precursory material, we manufactured highly ordered IO-FTO films with large domain size similar to that in Figure 2.

Interestingly, for IO-FTO with overlayers, when the heating rate during calcinations is faster than 2 °C/min, nanotube-like structure can be obtained on the top of the IO-FTO, as illustrated in Figure 4. Figure 4a shows SEM image of FTO nanotubes formed due to the overlayer on the IO-FTO film. Figure 4b presents a high-magnification SEM image of FTO nanotubes on top of the as-synthesized IO-FTO film. The average diameter of the nanotubes is about 300 nm, and the wall thickness is approximately 15 nm.

A hypothetical growth mechanism resulting in the FTO tubular structure, termed as "secondary template" growth mechanism is also illustrated in Scheme 1(d, e). Here the PS spheres serve as the primary template forming the IO-FTO structures

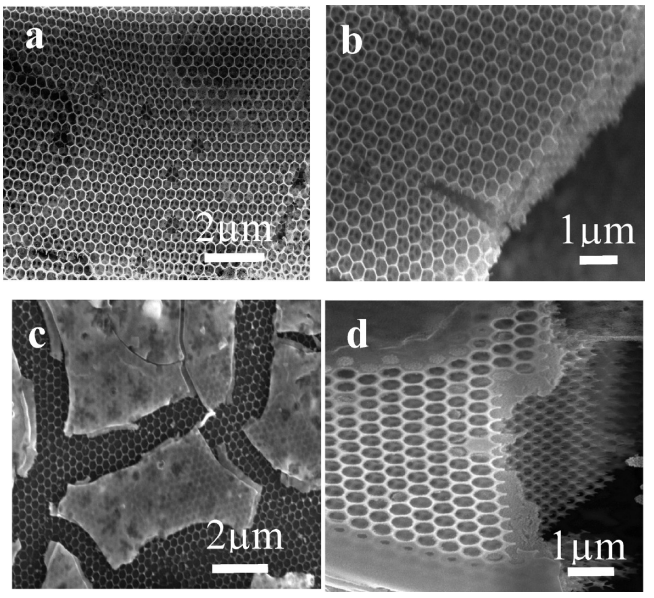

Figure 3. SEM images of as-prepared inverse opal FTO under different condition. (a) Insufficient infiltration of the precursory material results a compact but thin, with few cracks IO-FTO film. (b) Cross-section SEM image of the IO-FTO film with insufficient filtration of precursory materials. (c) Excessive infiltration of precursory material results a thicker film but with flake-like overlayers covering the top layer. (d) Cross-section SEM image of the IO-FTO film with excessive filtration of precursory materials.

upon the decomposition of PS spheres in air. Obviously, the development of FTO hexagonally porous structure starts at the top layers where the PS spheres in direct contact with air, burn off first. For the lower layers, the gaseous species, e.g. CO_2 and H_2O, will be temporarily belated in the hexagonal voids under the top overlayer. The build-up of the gas pressure in the voids will eventually pop up and clear the overlayer, forming the hexagonal array of holes (secondary template) to sustain the gas flow, which is shown in Scheme 1d. The morphology of this secondary template depends on the shape of the primary template, i.e., the hexagonal voids underneath the top layer. In this process the heating rate must be fast enough to quickly build-up a threshold pressure that is high enough to pop up the overlayer. At slow heating rates (1 °C/min), which provides enough time for gases to diffuse through the pore network, we did not observe any tubular structures.

After the secondary template is formed, the additional gas from deeper layers goes preferentially through the open holes, where it encounters less flow resistance. The FTO precursory material in the proximity of the open holes is transported by this directed gas flow to form the tubular structure, as shown in Scheme 1e. The proposed scenario is supported by the fact that all the nanotubes are only found on the top of the IO-FTO structure covered with overlayers. The length of the nanotubes is limited by the available precursory materials supplied by the overlayer. However, in thicker overlayer that provides more materials for growing longer tubes, the initial gas pressure may not be high enough to pop it up. Hence, the "secondary template" growth of nanotubes could have some limitations but it definitely provides a novel approach for nanomaterials synthesis.

Figure 5 shows the X-ray diffraction (XRD) pattern of the as-synthesized 3-D IO-FTO films on glass, which were calcinated at

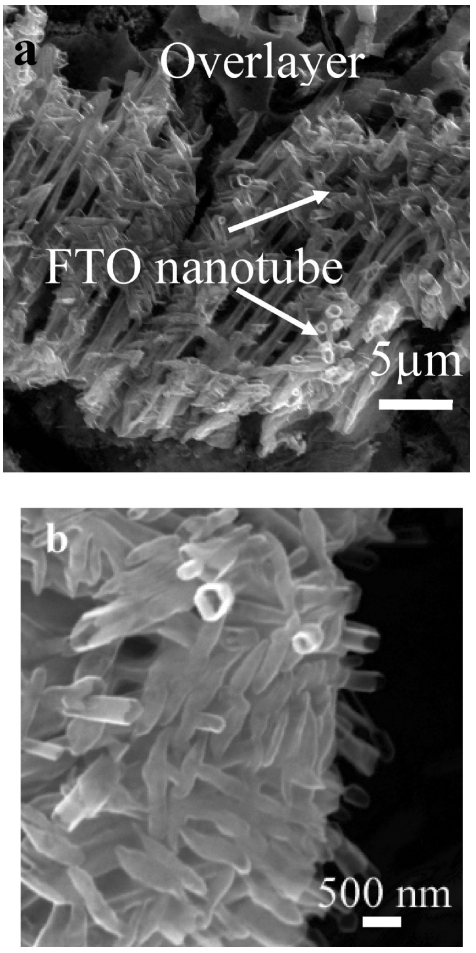

Figure 4. SEM images of the FTO nanotubes formed on the very top of 3-D inverse opal FTO films: (a) low and (b) high magnification.

500 °C. For comparison, the XRD of a commercial FTO glass is also shown. The XRD measurements indicate that our IO-FTO films have the tetragonal rutile structure in polycrystalline configuration.[52] The XRD spectra contain all peaks characteristic for SnO_2 (JCPDS Powder Diffraction File Card 5−0467). For example, the more intense diffraction peaks for the IO-FTO film at 28.7, 36.5, 53.8, and 66.1° correspond to at ⟨110⟩, ⟨101⟩, ⟨211⟩, ⟨301⟩ planes, respectively, in good agreement with the diffraction peaks found in the commercial FTO thin film, as well as other literatures.[44,53,54] The peaks become broader than those in the commercial FTO film due to the smaller grain size of our IO-FTO. This is indicated by the mean grain size of ∼24 nm in our IO-FTO as estimated using Scherrer equation from the full width at half-maximum (FWHM) of the XRD peaks. The XRD of our IO-FTO films does not show any impurity peaks, indicating the high purity of the as-synthesized films.

Optical Properties. To elucidate peculiarities of the optical properties due to the photonic-crystal structure in our samples, we conducted the spectroscopic study in the UV−vis region on the as-synthesized 3-D IO-FTO films using the commercial FTO glass as a reference.

Figure 6 shows the UV−vis transmittance spectra of the IO-FTO films and a commercial flat FTO-coated glass for the incident light perpendicular to the film plane. Apparently, the IO-FTO films exhibit much stronger loss in the region of 400−600 nm than the reference FTO film. This can be attributed

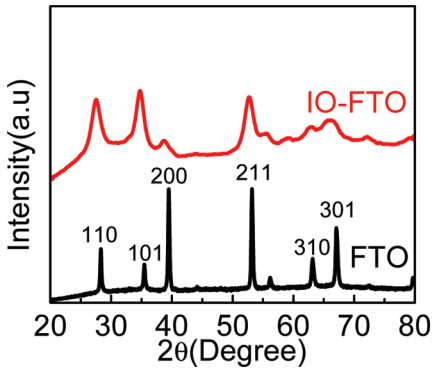

Figure 5. XRD spectra of a commercial FTO glass as a reference (black, denoted as FTO); 3D inverse opal FTO film prepared on a regular glass substrate (red, denoted as IO-FTO) and the calcination temperature for this sample is at 500 °C.

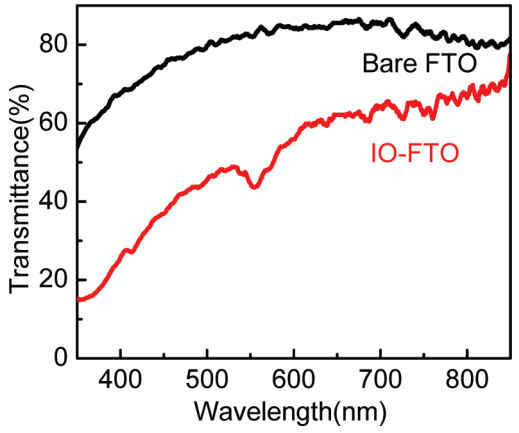

Figure 6. Transmittance spectra of 3D FTO inverse opal film on commercial bare FTO glass (red) and commercial bare planar FTO glass (black).

to a longer optical path in the 3D IO-FTO representing a photonic crystal with a period of 300 nm. This extension of optical path in 3D IO-FTO is expected because of the multiple scattering[55] when the wavelength of incident light is comparable with the optical periodicity of the crystal.

Furthermore, because a 3D inverse opal photonic crystal can strongly diffract light of a wavelength close to the crystal periodicity, there should be a stop band that excludes the passage of photons of the appropriate range of frequencies.[47,49] In our 3D IO-FTO, the stop-band was found at 560 nm as measured for the perpendicular incident light. This value is in good agreement with the estimation of 566 nm obtained from the Bragg formula[49]

$$\lambda = 1.633d(\varphi n_{\text{walls}} + (1-\varphi)n_{\text{voids}})$$

Here d is the diameter of the spheres (300 nm in our case), n_{wall} and n_{voids} are refractive indices of the wall material and voids, respectively, and $\varphi = 0.26$ is the solid volume fraction for inverse FCC structure. The effective refractive indices are about ~1.6 for the wall material (FTO)[56] and 1 for the air in the voids.

Electrical Properties. The nominal sheet resistance of the IO-FTO films on commercial continuous FTO glass was characterized by a four-probe resistance measurement method. For the set of our IO-FTO films with different thickness (0.5, 0.8, 1.5, 2.5, and 3.5 μm) it was 7.11, 7.43, 8.07, 8.10, and 8.72 Ω/□,

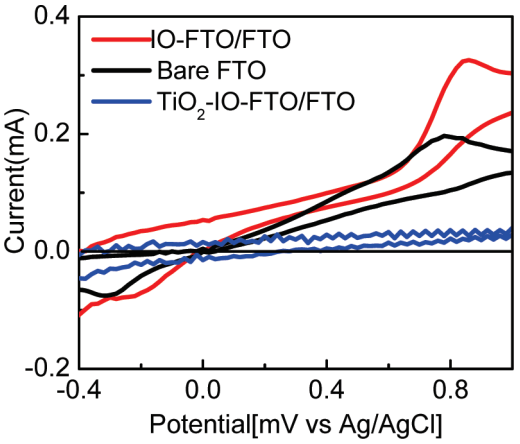

Figure 7. Cyclic voltammetry of ferrocene using IO-FTO/FTO (red), planar FTO (black) and TiO_2/IO-FTO/FTO (blue) as working electrodes at a scan rate of 50 mV/s. Herein, IO-FTO/FTO represents the 3D IO-FTO on a commercial planar FTO glass, TiO_2/IO-FTO/FTO represents the surface-passivated IO-FTO/FTO sample by an ALD TiO_2 layer, and bare FTO represents a commercial planar FTO glass.

respectively. These values are only slightly higher than ~6.47 Ω/□ of the commercial FTO film, which shows that our IO-FTO on a continuous FTO film possesses comparable conductivity as the commercial continuous FTO film. The sheet resistance measurement suggests that the presence of the IO-FTO layer atop the continuous flat FTO layer only slightly increased the overall resistance. This can be understood with Ohm's law: the majority current flow in the IO-FTO layer must be through the pathways with lowest resistance, that is, the normal direction of the IO-FTO layer. Thus, the voids and the inevitable cracks in the IO-FTO layer that can cause large resistance in the lateral direction, will not affect the collection of current. Cracks in thin films always form preferentially along the film normal (it is unlikely that a crack can slice the film) so as to decrease the lateral conductance. For comparison, a continues and compact FTO film made by spraying of the same precursory solution on a bare glass substrate shows a sheet resistance of ~10 Ω/□, close to the commercial FTO glass To be clear, we emphasize hereby that a continuous FTO layer underneath the IO-FTO layer is necessary for final current collection, while the IO-FTO structure provides shortcuts (in vertical direction) to transport charges to this continuous FTO layer.

We further characterized the type of carriers in our IO-FTO structures fabricated on the bare glass substrates by measuring the Hall effect polarity. The polarity of the Hall voltage coincides with that of a commercial n-type Si sample of the same geometry measured with the same setup which confirms that our IO-FTO samples are n-type. This assures that the IO-FTO prepared by our method is suitable for applications in which n-type TCO is desired.

To demonstrate the feasibility of our IO-FTO films for use in optoelectronic devices, such as solar cells, it is necessary to show that all the surfaces of our IO-FTO film can be coated with a semiconducting layer. The study of dye-sensitized solar cells (DSSCs) showed that the coverage of the FTO surface with a charge blocking semiconductor layer is crucial to minimize shunt current, which results in an internal short circuit between the anode and cathode) and can lead to a significant loss of the

output power.[17,20,57−59] In contrast to a 2D planar FTO film, it is exceptionally difficult to achieve a full surface coverage of the 3D FTO electrode architecture with a charge blocking layer using conventional deposition techniques. We, therefore, employed a state-of-the-art atomic layer deposition (ALD) method to coat all the surface of our IO-FTO film with a layer of TiO_2.[60] To investigate the functionality of this ALD TiO_2 layer as an electron blocking layer, the cyclic voltammetry (CV) study of the ferrocene (Fc/Fc^+) redox reaction[57] was conducted using the TiO_2 coated IO-FTO film as working electrode. Figure 7 shows the CV curves of the Fc/Fc^+ redox reaction for a 2D planar FTO, our IO-FTO (without ALD TiO_2), and the ALD TiO_2-coated IO-FTO, respectively. It can be seen that the redox current of ~0.32 mA on the IO-FTO/FTO electrode is noticeably higher than that on a bare commercial FTO. This is defined by the larger surface area of the 3-D IO-FTO/FTO available for the redox species as compared to the commercial planar FTO electrode. Remarkably, after the ALD coating of an amorphous TiO_2 layer on the IO-FTO, the current decreased to only a few microamperes, indicating an excellent coverage of TiO_2 on nearly all surface of the IO-FTO electrodes by the ALD technique. This confirms that a 10 nm thick TiO_2 blocking layer can efficiently suppress shunt leakage at the FTO/TiO_2 and FTO/electrolyte interfaces. Our results prove that the prepared IO-FTO structures can be used as photocurrent collecting electrodes in photovoltaic devices with potentially short charge transport distances and enhanced light harvesting due to multiple light scattering in the photonic crystal structures.

CONCLUSIONS

In summary, we have demonstrated the synthesis of highly ordered 3D inverse opal FTO electrodes using a facile, template-based, solution chemistry methodology. The as-synthesized IO-FTO electrodes exhibit a large surface roughness factor of more than 60, which is desirable for enhanced charge transport in photovoltaic devices. The IO-FTO electrodes show strong light scattering in the visible region and a pronounced photonic stop band at 560 nm. These properties are potentially valuable for enhanced light harvesting via multiple light scattering in the inverse opal structures. Hall Effect measurements indicate that the as-synthesized IO-FTO films are n-type semiconductors. The IO-FTO films on a planar FTO glass exhibit excellent conductivity in the vertical direction and a nominal sheet resistance less than 10 Ω/square. Using the atomic layer deposition method, the entire surface of the IO-FTO electrode can be readily covered with a layer of amorphous TiO_2. Cyclic voltammetric study suggests that this thin ALD TiO_2 layer acts as an effective electron blocking layer, which is crucial for the suppression of shunt leak in photovoltaic applications such as dye-sensitized solar cells.

ASSOCIATED CONTENT

Supporting Information. The calculation on the surface roughness factor for n-layer FCC-packed spheres. This material is available free of charge via the Internet at http://pubs.acs.org/

AUTHOR INFORMATION

Corresponding Author
*E-mail: txu@niu.edu.

ACKNOWLEDGMENT

We thank the U.S. Department of Energy for financial support under Contract DE-AC02-06CH11357 and the NIU-Argonne Graduate NanoScience Fellowship through InSET. The electron microscopy was conducted at the Electron Microscopy Center for Materials Research at Argonne National Laboratory, a U.S. Department of Energy Office of Science Laboratory operated under Contract DE-AC02-06CH11357 by UChicago Argonne, LLC.

REFERENCES

(1) (a) Ginley, D. S.; Bright, C *MRS Bull.* **2000**, *25*, 15. (b) Lewis, B. G.; Paine, D. C. *MRS Bull.* **2000**, *25*, 22.
(2) Haacke, G. *Annu. Rev. Mater. Sci.* **1977**, *7*, 73.
(3) Granqvist, C. G. *Sol. Energy Mater. Sol. Cells* **2007**, *91*, 1529.
(4) Edwards, P. P.; Porch, A.; Jones, M. O.; Morgan, D. V.; Perks, R. M. *Dalton Trans.* **2004**, 2995–3002.
(5) Hamberg, I.; Granqvist, C. G. *J. Appl. Phys.* **1986**, *60*, R123–R159.
(6) Hoel, C. A.; Mason, T. O.; Gaillard, J.-F.; Poeppelmeier, K. R. *Chem. Mater.* **2010**, *22*, 2569–3579.
(7) Rauf, I. A. *Mater. Lett.* **1993**, *18*, 123–127.
(8) Wang, A.; Babcock, J. R.; Edleman, N. L.; Metz, A. W.; Lane, M. A.; Asahi, R.; Dravid, V. P.; Kannewurf, C. R.; Freeman, A. J.; Marks, T. J. *Proc. Natl. Acad. Sci.* **2001**, *98*, 7113–7116.
(9) Armstrong, N. R.; Veneman, P. A.; Ratcliff, E.; Placencia, D.; Brumbach, M. *Acc. Chem. Res.* **2009**, *42*, 1748–1757.
(10) Walzer, K.; Maennig, B.; Pfeiffer, M.; Leo, K. *Chem. Rev.* **2007**, *107*, 1233.
(11) Yang, Z.; Xu, T.; Y., I.; Welp, U.; Kwok, W. K. *J. Phys. Chem. C* **2009**, *113*, 20521–20526.
(12) Hamann, T. W.; Jensen, R. A.; Martinson, A. B. F.; van Ryswyk, H.; Hupp, J. T. *Energy Environ. Sci.* **2008**, *1*, 66–78.
(13) Martinson, A. B. F.; Hamann, T. W.; Pellin, M. J.; Hupp, J. T. *Chem.—Eur. J.* **2008**, *14*, 4458–4467.
(14) Yang, Z.; Xu, T.; Gao, S.; Welp, U.; Kwok, K. W. *J. Phys. Chem. C* **2010**, *114*, 19151–19156.
(15) Rühle, S.; Dittrich, T. *J. Phys. Chem. B* **2005**, *109*, 9522–9526.
(16) van de Lagemaat, J.; Park, N.-G.; Frank, A. J. *J. Phys. Chem. B* **2000**, *104*, 2044–2052.
(17) Juan Bisquert, J.; Garcia-Belmonte, G.; Fabregat-Santiago, F. *J Solid State Electrochem.* **1999**, *3*, 337–347.
(18) Rühle, S.; Cahen, D. *J. Phys. Chem. B* **2004**, *108*, 17946–17951.
(19) Hwang, I.; McNeill, C. R.; Greenhama, N. C. *J. Appl. Phys.* **2009**, *106*, 094506.
(20) Kopidakis, N.; Park, E. A. S.-G.; van de Lagemaat, J.; Frank, A. J. *J. Phys. Chem. B* **2000**, *104*, 3930–3936.
(21) Peter, L. *Acc. Chem. Res.* **2009**, *42*, 1839–1847.
(22) Brédas, J. L.; Norton, J. E.; Cornil, J.; Coropceanu, V. *Acc. Chem. Res.* **2009**, *42*, 1691–1699.
(23) Peter, L. M. *J. Phys. Chem. C* **2007**, *111*, 6601–6612.
(24) Peter, L. M. *Phys. Chem. Chem. Phys.* **2007**, *9*, 2630–2642.
(25) Kron, G.; Egerter, T.; Werner, J. H.; Rau, U. *J. Phys. Chem. B* **2009**, *107*, 3556–3564.
(26) Shockley, W.; Queisser, H. J. *J. Appl. Phys.* **1961**, *32*, 510–519.
(27) Tisdale, W. A.; Williams, K. J.; Timp, B. A.; Norris, D. J.; Aydil, E. S.; Zhu, X.-Y. *Science* **2010**, *328*, 1543–1547.
(28) Shankar, K.; Basham, J. I.; Allam, N. K.; Varghese, O. K.; Mor, G. K.; Feng, X.; Paulose, M.; Seabold, J.; Choi, K.-S.; Grimes, C. A. *J. Phys. Chem. C* **2009**, *113*, 6327–6359.
(29) Law, M.; Greene, L. E.; Johnson, J. C.; Saykally, R.; Yang, P. D. *Nat. Mater.* **2005**, *4*, 455–459.
(30) Martinson, A. B. F.; Goes, M. S.; Fabregat-Santiago, F.; Bisquert, J.; Pellin, M. J.; Hupp, J. T. *J. Phys. Chem. A* **2009**, *113*, 4015–4021.
(31) Zhu, K.; Neale, N. R.; Miedaner, A.; Frank, A. J. *Nano Lett.* **2007**, *7*, 69–74.

(32) Jin, W.-M.; Shin, J.-H.; Cho, C.-Y.; Kang, J.-H.; Park, J. H.; Moon, J. H. *ACS Appl. Mater. Interfaces* **2010**, *2*, 2970–2973.
(33) Taranekar, P.; Qiao, Q.; Jiang, H.; Ghiviriga, I.; Schanze, K. S.; Reynolds, J. R. *J. Am. Chem. Soc.* **2007**, *129*, 8958–8959.
(34) Martinson, A. B. F.; Elam, J. W.; Liu, J.; Pellin, M. J.; Marks, T. J.; Hupp, J. T. *Nano Lett.* **2008**, *8*, 2862–2866.
(35) Kavan, L.; Grätzel, M.; Gilbert, S. E.; Klemenz, C.; Schell, H. J. *J. Am. Chem. Soc.* **1996**, *118*, 6716–6723.
(36) Forro, L.; Chauvet, O.; Emin, D.; Zuppiroli, L.; Berger, H.; Lévy, F. *J. Appl. Phys.* **1994**, *75*, 633.
(37) Wagner, P.; Helbig, R. *J. Phys. Chem. Solids* **1974**, 35.
(38) Mora-Sero, I.; Fabregat-Santiago, F.; Denier, B.; Bisquert, J.; Tena-Zaera, R.; Elias, J.; Levy-Clement, C. *Appl. Phys. Lett.* **2006**, *89*, 203117.
(39) Zhu, X.-Y.; Yang, Q.; Muntwiler, M. *Acc. Chem. Res.* **2009**, *42*, 1779–1787.
(40) Li, Y. Z.; Kunitake, T.; Fujikawa, S. *J. Phys. Chem. B* **2006**, *110*, 13000–13004.
(41) Nishimura, S.; Abrams, N.; Lewis, B. A.; Halaoui, L. I.; Mallouk, T. E.; Benkstein, K. D.; van de Lagemaat, J.; Frank, A. J. *J. Am. Chem. Soc.* **2003**, *125*, 6306–6310.
(42) Tao, C.; Zu, W.; An, Q.; Li, G. *J. Phys. Chem. C* **2010**, *114*, 10641–10647.
(43) Aouaj, M. A.; Diaz, R.; Belayachi, A.; Rueda, F.; Abd-Lefdil, M. *Mater. Res. Bull.* **2009**, *44*, 1458–1461.
(44) Kawashima, T.; Ezure, T.; Okada, K.; Matsui, H.; Goto, K.; Tanabe, N. *J Photoch Photobio A* **2004**, *164*, 199–202.
(45) Xie, H.; Li, Y.; Jin, S.; Han, J.; Zhao, X. *J. Phys. Chem. C* **2010**, *114*, 9706–9712.
(46) Xia, J.; Masaki, N.; Jiang, K.; Yanagida, S. *J. Phys. Chem. B* **2006**, *110*, 25222–25228.
(47) Turner, M. E.; Trentler, T. J.; Colvin, V. L. *Adv. Mater.* **2001**, *13*, 180–183.
(48) Jiang, P.; Bertone, J. F.; Colvin, V. L. *Science* **2001**, *291*, 453–457.
(49) Hatton, B.; Mishchenko, L.; Davis, S.; Sandhage, K. H.; Aizenberg, J. *Proc. Natl. Acad. Sci. U.S.A.* **2010**, *107*, 10354–10359.
(50) Fujihara, S.; Maeda, T.; Ohgi, H.; Hosono, E.; Imai, H.; Kim, S.-H. *Langmuir* **2004**, *20*, 6476–6481.
(51) Waterhouse, G. I. N.; Metson, J. B.; Idriss, H.; Sun-Waterhouse, D. *Chem. Mater.* **2008**, *20*, 1183–1190.
(52) Guldin, S.; Huttner, S.; Kolle, M.; Welland, M. E.; Muller-Buschbaum, P.; Friend, R. H.; Steiner, U.; Tetreault, N. *Nano Lett.* **2010**, *10*, 2303–2309.
(53) Martinez, A. I.; Huerta, L.; de Leon, J. M. O. R.; Acosta, D.; Malik, O.; Aguilar, M. *J. Phys. D: Appl. Phys.* **2006**, *39*, 5091–5096.
(54) Ramaiah, K. S.; Raja, V. S. *Appl. Surf. Sci.* **2006**, *253*, 1451–1458.
(55) Mihi, A.; Miguez, H. J. *Phys. Chem. B.* **2005**, *109*, 15968–15976.
(56) Smith, A.; Laurent, J. M.; Smith, D. S.; Bonnet, J. P.; Clemente, R. R. *Thin Solid Films* **1995**, *266*, 20–30.
(57) Li, H.; Jiang, B.; Schaller, R.; Wu, J.; Jiao, J. *J. Phys. Chem. C* **2010**, *114*, 11375–11380.
(58) Ito, S.; Liska, P.; Comte, P.; Charvet, R.; Péchy, P.; Bach, U.; Schmidt-Mende, L.; Zakeeruddin, S. M.; Kay, A.; Nazeeruddin, M. K.; Grätzel, M. *Chem. Commun.* **2005**, 4351–4351.
(59) Junghänel, M.; Tributsch, H. *J. Phys. Chem. B* **2005**, *109*, 22876–22883.
(60) George, S. M. *Chem. Rev.* **2010**, *110*, 111–131.